NIIZEKI, K. (1989). *J. Phys. A*, **22**, 193–204.
PLEASANTS, P. A. B., BAAKE, M. & ROTH, J. (1994). Tübingen preprint TPT-QC-94-05-1. Univ. Tübingen, Germany.
RADULESCU, O. (1993). *J. Phys. I Fr.* **3**, 2099–2113.
RADULESCU, O. (1994). Thèse, Univ. de Paris Sud, France.
ROKSHAR, D. S., MERMIN, N. D. & WRIGHT, D. C. (1987). *Phys. Rev. B*, **35**, 5487.
SINGH, A. & RANGANATHAN, S. (1993). *J. Non-Cryst. Solids*, **153 & 154**, 86–91.
SUTTON, A. P. & BALLUFFI, R. W. (1987). *Acta Metall.* **35**, 2177–2201.
WARRINGTON, D. H. (1988). *Quasicrystalline Materials*, edited by C. JANOT & J. M. DUBOIS, p. 243. Singapore: World Scientific.
WARRINGTON, D. H. (1992). Colloque Quasicristaux, Meudon, France.
WARRINGTON, D. H. (1993*a*). Colloque Quasicristaux, Grenoble, France.
WARRINGTON, D. H. (1993*b*). Colloque Quasicristaux, Thessaloniki. *Mater. Sci. Forum*, **126–128**, 57–60.
WARRINGTON, D. H. & BUFFALINI, P. (1971). *Scr. Metall.* **5**, 771–776.

Acta Cryst. (1995). A**51**, 343–350

Models for Termination of Crystal Boundaries in the Theory of Transmission Electron Diffraction and Comparison with Experimental Data

BY N. GRIGORIEFF* AND D. CHERNS

H. H. Wills Physics Laboratory, University of Bristol, Tyndall Avenue, Bristol BS8 1TL, England

A. R. PRESTON

Department of Materials Science and Metallurgy, University of Cambridge, Pembroke Street, Cambridge CB2 3QZ, England

AND M. J. YATES

BT Laboratories, Martlesham Heath, Ipswich IP5 7RE, England

(*Received* 9 *June* 1994; *accepted* 31 *October* 1994)

Abstract

Calculations of electron diffraction intensities in transmission electron microscopy commonly assume a model representing surfaces and interfaces in crystals as flat boundaries (flat-boundary model, FBM). It is shown that the independent-atom model (IAM) representing the crystal potential as a superposition of spherical atomic potentials leads to improved boundary conditions. Intensities calculated from the two models at large deviation from the Bragg peak in weak reflections (*e.g.* 200 in InGaAs) differ significantly. Results from both types of calculation are compared with an experimental diffraction pattern recorded using energy-filtered large-angle convergent-beam electron diffraction from an $In_{0.53}Ga_{0.47}/InP$ bicrystal. It is shown that calculations using the IAM give a better agreement with experiment.

1. Introduction

Calculations of electron diffraction intensities from thin crystals in transmission electron microscopy (TEM) usually assume a sharp cut-off of the crystal potential at surfaces and sharp transitions of the potential at interfaces inside the sample. This leads to a convenient set of boundary conditions that can be used in dynamical theory (see Peng & Whelan, 1990*a*, for a recent review). The effects of contamination and the detailed three-dimensional atomic structure of surfaces and interfaces are generally ignored owing to their small contribution to the total volume of the crystal. Earlier attempts at understanding the effect of boundary conditions in multislice calculations have been made for forbidden reflections (Stobbs, Boothroyd & Stobbs, 1989; Gipson, Lanzerotti & Elser, 1989). Here, we report a different representation of the crystal potential which pays more attention to the spatial variation of the potential at the atomic level at interfaces and surfaces. This leads to a significantly improved agreement between calculated and observed intensities in cases where the reflection under consideration is weak, such as the 200 reflection from InGaAs. Contamination is still assumed to play a minor role and is ignored in the calculations.

2. The crystal potential at surfaces and interfaces

In an infinite perfect crystal, the potential can be represented by a Fourier series (Bethe, 1928). Discontinuities at surfaces and interfaces perturb the potential inside the bulk. However, it is usually assumed that these perturbations are confined to a small volume and that the potential in the bulk is unchanged. Thus, the situation can

*Present address: MRC Laboratory of Molecular Biology, Hills Road, Cambridge CB2 2QH, England.

be simplified by setting the potential inside the bulk to that of an infinite crystal and to zero outside the crystal, such that the potential in any part of the crystal may be represented as a Fourier series. This treatment results in two-dimensional flat boundaries separating different parts of the sample, an approximation that will be referred to as the flat-boundary model (FBM). For the potential $V_{\rm FBM}$ in one part of the sample (*e.g.* in one layer if the sample consists of several flat layers),

$$V_{\rm FBM}(\mathbf{r}) = \left[\sum_g V_g \exp(-2\pi i \mathbf{g}\cdot\mathbf{r})\right] S(\mathbf{r}). \qquad (1)$$

Here, $\mathbf{r}$ is the real-space coordinate, $S(\mathbf{r})$ is a shape function, V_g is the Fourier coefficient for reflection $\mathbf{g}$ and the sum over $\mathbf{g}$ includes all reflections. In semiconductors, the crystal potential derived from tabulated atomic form factors (Doyle & Turner, 1968) is widely used and experimentally observed deviations due to bonding are small (*e.g.* Zuo, Spence & O'Keeffe, 1988). Thus, V_g can be calculated from the sum of (relativistic) form factors f_i for atoms i in one unit cell:

$$V_g = [h^2/2\pi m e \Omega] \sum_{\rm unit\ cell} f_i(\theta) \exp(-2\pi i \mathbf{g}\cdot\mathbf{r}_i) \times \exp(-B_i g^2/4) \qquad (2)$$

where h is Planck's constant, Ω is the unit-cell volume, m is the relativistic mass of the electron, e is the elementary charge, θ is the scattering angle, $B_i = 8\pi^2\langle\Delta_i^2\rangle$ is the Debye–Waller factor for atom i with mean square displacement $\langle\Delta_i^2\rangle$ and $\mathbf{r}_i$ is the coordinate for atom i. For a parallel-sided crystal slab infinite in two dimensions (taken as x and y) and of thickness T along z, $S(\mathbf{r})$ can be defined as

$$S(\mathbf{r}) = \begin{cases} 1 & -T/2 \le z \le T/2 \\ 0 & \text{otherwise.} \end{cases} \qquad (3)$$

Then, the Fourier transform of (1) is

$$V_{\rm FBM}(\mathbf{q}) = \left[\sum_g v_g \delta(\mathbf{q}-\mathbf{g})\right] * S(\mathbf{q}) \qquad (4)$$

with the shape transform

$$S(\mathbf{q}) = \delta(\mathbf{q}_{xy}) \sin(\pi T q_z)/\pi q_z c, \qquad (5)$$

where $\mathbf{q}$ is a reciprocal-space coordinate, c is the magnitude of the unit-cell vector along $\mathbf{z}$ and $*$ denotes a convolution. Equation (4) contains a sum of δ functions at the reciprocal-lattice points weighted by the Fourier coefficients V_g of the potential. The convolution of the δ functions with $S(\mathbf{q})$ causes the reciprocal-lattice points to be elongated in the z direction.

The simplification made in (1) is illustrated in Fig. 1(*a*) using the crystal surface as an example. As a result of the sharp transition from the bulk potential to vacuum, part of the crystal potential produced by individual atoms inside the crystal is omitted and part of the potential produced by atoms that would be included in an infinite crystal is added to the potential of the finite crystal.

The independent-atom model (IAM) normally used in gas-phase electron diffraction (*e.g.* Hargittai, 1988) approximates the total crystal potential by the superposition of neutral spherical-atom potentials, thereby neglecting charge redistribution due to chemical bonding. A similar formulation has been used for the study of imperfect crystals and is called the rigid-ion approximation (*e.g.* Anstis & Cockayne, 1979). According to the IAM, the potential near a boundary deviates from that of the infinite crystal. This is illustrated again for the crystal surface in Fig. 1(*b*). To represent this situation, we write for the potential $V_{\rm IAM}$ in a homogeneous region of the sample (*e.g.* one layer of a multilayer sample)

$$V_{\rm IAM}(\mathbf{r}) = V_{\rm cell}(\mathbf{r}) * \left[S(\mathbf{r})\sum_{\mathbf{R}}\delta(\mathbf{r}-\mathbf{R})\right]. \qquad (6)$$

$\mathbf{R}$ is a lattice vector and the infinite sum over $\mathbf{R}$ is restricted by the shape function $S(\mathbf{r})$. $V_{\rm cell}(\mathbf{r})$ is the sum of atomic potentials $V_i(\mathbf{r})$ over one unit cell defined as

$$V_{\rm cell}(\mathbf{r}) = \sum_{\rm unit\ cell} V_i(\mathbf{r}). \qquad (7)$$

Thus, we have a crystal lattice represented by a sum of δ functions in (6) and a unit cell placed at each lattice point by means of a convolution. This treatment assumes the sample is an integral number of unit cells thick. It is easily extended to deal with half unit cells by redefinition

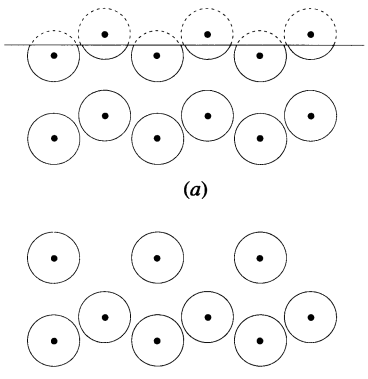

Fig. 1. Two different models for the crystal surface. Atoms are represented as dots with a circle to indicate an extended atomic potential. (*a*) A flat crystal surface is assumed with a boundary line marking a sharp cut through the atomic potential. The dashed lines indicate parts of the potential lying outside this boundary. Those parts are assumed to be zero according to the FBM. Thus, for some atoms inside the boundary a part of the potential would be omitted and some other parts of the potential of atoms outside the boundary would be included in the crystal. (*b*) the IAM suggests a different situation in which only complete atoms are allowed. This means that the complete potential of atoms inside the boundary is included in the crystal structure and there is no atom outside the boundary that partially contributes to the total potential.

of the cell. In (6), contrary to (1), $S(\mathbf{r})$ does not truncate the potential of individual atoms inside the crystal. For simplicity we have assumed in (6) a crystal with a thickness T equal to an odd number N of unit cells, such that the middle of the lattice coincides with a lattice point which we take to be the origin. Then $T = Nc$ and the Fourier transform of (6) is

$$V_{\mathrm{IAM}}(\mathbf{q}) = V_{\mathrm{cell}}(\mathbf{q})\left[S(\mathbf{q}) * \sum_g \delta(\mathbf{q}-\mathbf{g})\right]. \quad (8)$$

Analogous to (2),

$$V_{\mathrm{cell}}(\mathbf{q}) = (h^2/2\pi me\Omega) \sum_{i \in \text{unit cell}} f_i(\theta) \times \exp(-2\pi i \mathbf{q}\cdot\mathbf{r}_i)\exp(-B_i q^2/4). \quad (9)$$

Thus,

$$V_{\mathrm{cell}}(\mathbf{g}) = V_g. \quad (10)$$

For a plate-like crystal with $S(\mathbf{r})$ defined in (3), the Fourier transform (8) becomes

$$\begin{aligned} V_{\mathrm{IAM}}(\mathbf{q}) &= V_{\mathrm{cell}}(\mathbf{q})\sum_g \delta(\mathbf{q}_{xy}-\mathbf{g}_{xy}) \\ &\quad \times \sin[\pi(q_z - g_z)Nc]/\pi(q_z - g_z)c \\ &= [\sin(\pi q_z Nc)/\sin(\pi q_z c)] \\ &\quad \times \sum_{g_{xy}} V_{\mathrm{cell}}(\mathbf{g}_{xy}+\mathbf{q}_z)\delta(\mathbf{q}_{xy}-\mathbf{g}_{xy}), \end{aligned} \quad (11)$$

where the sum over g_z in the first line of (11) has been replaced by the sine term in the second line. This derivation is expanded in the Appendix. We may now compare the two transforms (4) and (8). For a wave-vector transfer $\mathbf{q} = \mathbf{g}$ ($\mathbf{g}$ exactly excited), the two potentials V_{FBM} and V_{IAM} are the same. We may see this by writing the difference of the two transforms (4) and (8) as

$$\Delta V(\mathbf{q}) = \sum_g \Delta V_g(\mathbf{q}) S(\mathbf{q}-\mathbf{g}) \quad (12)$$

with

$$\Delta V_g(\mathbf{q}) = V_{\mathrm{cell}}(\mathbf{q}) - V_g. \quad (13)$$

For a plate-like crystal of thickness $T = Nc$, the shape transform $S(\mathbf{q}-\mathbf{g}) = 0$ if $\mathbf{q}-\mathbf{g} = \mathbf{g}'$, where $\mathbf{g}'$ is another reciprocal-lattice vector [see (5)] and the sum in (12) reduces to one term whose coefficient ΔV_g is zero according to (10), making the two Fourier transforms coincide. Hence, if we consider only one strongly excited beam and the transmitted beam (two-beam approximation), we expect the dynamical scattering amplitudes according to the two models to be the same.

If a reflection is only weakly excited, we write for the wave-transfer vector $\mathbf{q} = \mathbf{g} + \mathbf{s}$, where $\mathbf{s}$ is the deviation parameter. For a plate-like crystal, $\mathbf{s}$ is parallel to the bottom surface normal $\mathbf{n}$ which points away from the crystal and, therefore, $\mathbf{s} = s\mathbf{n}$. We use the kinematical approximation and write, for the scattered amplitude $\varphi_{g,\mathrm{FBM}}$ according to the FBM,

$$\varphi_{g,\mathrm{FBM}}(s) = \sum_{g_z} F_g \sin[\pi T(g_z + s)]/\pi(g_z + s)c \quad (14)$$

with

$$F_g = (2\pi me\Omega/h^2)V_g, \quad (15)$$

the structure factor for reflection $\mathbf{g}$. The sum over g_z in (14) runs over all reflections lying in the same reciprocal-lattice rod as $\mathbf{g}$ and thus may include higher-order Laue-zone (HOLZ) reflections. In the IAM, (14) becomes

$$\varphi_{g,\mathrm{IAM}}(s) = F(\mathbf{g}+\mathbf{s})\sin(\pi Ts)/\sin(\pi cs) \quad (16)$$

with $T = Nc$ and

$$F(\mathbf{g}+\mathbf{s}) = (2\pi me\Omega/h^2)V_{\mathrm{cell}}(\mathbf{g}+\mathbf{s}). \quad (17)$$

$F(\mathbf{g}+\mathbf{s})$ differs from the structure factor F_g only in that it describes the scattering of one unit cell for a wave-transfer vector $\mathbf{g}+\mathbf{s}$ rather than $\mathbf{g}$. The term $\sin(\pi Ts)/\sin(\pi cs)$ in (16) peaks at HOLZ reflections similar to the sum in (14), *i.e.* when $s = g_z$. Hence, the amplitude (16) includes all HOLZ reflections.

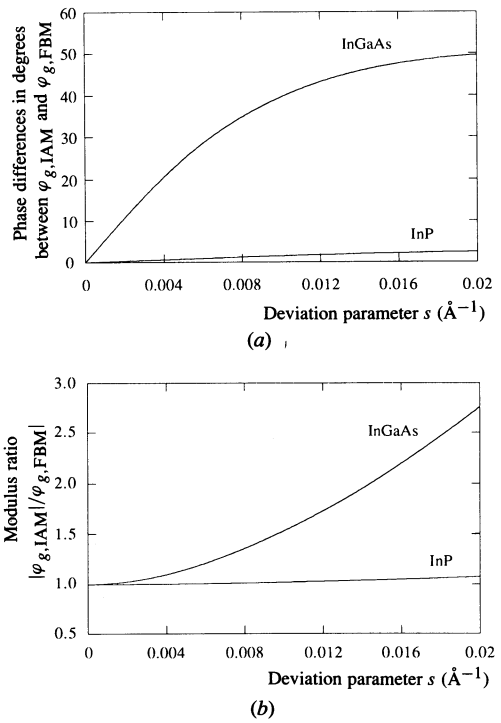

Fig. 2. Plots of (*a*) phase difference and (*b*) modulus ratio of scattered amplitudes for an $In_{0.53}Ga_{0.47}As$ and an InP crystal calculated using the IAM [equation (16)] and the FBM [equation (14)]. Phase difference and modulus ratio do not depend on the thickness of the sample. As can be seen, the two models give similar results for InP but deviate significantly for $In_{0.53}Ga_{0.47}As$.

The phase difference between amplitudes calculated using the two boundary models is shown in Fig. 2 for a 200 reflection in InP and $In_{0.53}Ga_{0.47}As$, together with their modulus ratio for $0 \leq s \leq 0.02\,Å^{-1}$. It can be seen that the two models deviate significantly in the case of $In_{0.53}Ga_{0.47}As$. The 200 reflection in $In_{0.53}Ga_{0.47}As$ is a factor of six weaker than in InP and small contributions from the changed potential at the surfaces have a large effect on the total scattering phase [Fig. 2(*a*)] and magnitude [Fig. 2(*b*)]. This is not the case for InP as can be seen in Fig. 2 from the small differences between the two models in phase and modulus. It is important to note here that the changes displayed in Fig. 2 do not depend on the total thickness of the crystal.

3. Experimental

To determine which of the two models described in the previous section gives a better representation of the true crystal potential, we should compare observed diffraction intensities with calculations using the two models. A method particularly suitable for recording diffraction patterns over a range of deviation parameters s is the large-angle convergent-beam electron diffraction (LACBED) technique (Tanaka, Saito, Ueno & Harada, 1980; Vincent, 1989). In convergent-beam electron diffraction (CBED), a convergent beam is incident on the sample. The diffraction pattern then consists of a number of displaced discs for each reflection visible in the back focal plane of the objective lens. If overlap of the discs is to be avoided, the convergence angle is restricted to the Bragg angle of the first-order reflection. However, by moving the sample away from the beam cross over as in LACBED, a diffraction pattern is generated in the image plane and the selected-area diffraction (SAD) aperture can be used to select one reflection. This allows much larger convergence angles (typically 6° is used). More importantly, the SAD aperture acts as an angular filter and thereby removes thermal diffuse scattering (TDS) to a large extent (Jordan, Rossouw & Vincent, 1991). Thus, even very weak diffraction intensities at large deviation parameters may be recorded with high accuracy.

Fig. 3 shows an example of a LACBED pattern. The disc shows detail up to very large deviation s. The pattern was obtained from a parallel-sided single-crystal slab with a thin buried layer in plan view. The modulation of the fringe intensity visible in the pattern is sensitive to the thin layer. Quantitative analysis yields thickness and composition of the thin layer to sub-monolayer accuracy (Grigorieff *et al.*, 1993). This type of work relies critically on accurate calculation of diffraction intensities as part of a curve-fitting procedure. Therefore, correct boundary conditions are of prime importance.

To test the two models it would, in principle, be possible to record a LACBED pattern from a single-crystal slab and compare the intensity envelope of the fringe maxima with calculated envelopes. For a parallel-sided slab, the envelope is a monotonically decreasing function for increasing deviation s. The two models predict different slopes for this envelope such that for increasing s intensity differences become larger [see Fig. 2(*b*)]. Hence, to detect differences in the slope, one would have to compare the intensity of fringes over a wide range of deviation parameters, which could lead to spurious results. For instance, the slope of the experimental pattern could be affected by the response function of the detector being not exactly linear. Another example is the averaging of LACBED contrast over a range of thicknesses due to rough sample surfaces. The effect of averaging would increase with deviation s thereby altering the slope of the fringe envelope. Although the surfaces can be expected to be very smooth (see below), it is more reliable to consider a modulated intensity envelope where the calculated intensity ratio of adjacent fringes will depend on the model. A suitable structure was found to be an $In_{0.53}Ga_{0.47}As$/InP bicrystal with surface normal (001), grown by metal-organic vapour-phase epitaxy (MOVPE) and a thickness ratio of the layers of 1:2. To ensure sufficient stability of the sample, the total thickness was chosen to be 1800 Å. A cross section of the structure is schematically shown in Fig. 4. In previous work (Jordan, Cherns, Hockly & Spurdens, 1989), it was demonstrated that the MOVPE growth method used here produces interfaces and surfaces of

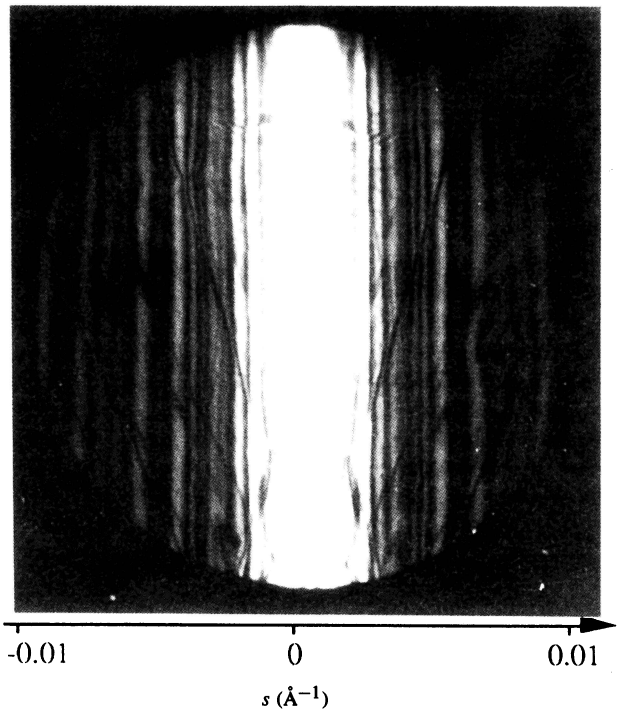

Fig. 3. A LACBED pattern in the 200 reflection from a 32 Å $In_{0.53}Ga_{0.47}As$ layer clad between 1500 Å of InP. Fringes are visible up to large values of the deviation parameter s.

near atomic smoothness. The $In_{0.53}Ga_{0.47}As$/InP bicrystal examined here was grown on an InP wafer and subsequently removed from the wafer using very selective etches (a mixture of H_2SO_4:H_2O_2:H_2O = 1:8:1 for $In_{0.53}Ga_{0.47}As$ and HCl for InP). This meant large parallel-sided crystal slabs, having typically an area of 1 mm^2, could be prepared without disrupting the interface or the surface smoothness. Thus, the sample quality was nearly ideal, allowing detailed comparison of experiment with theory.

A LACBED pattern in the 200 reflection was recorded on a 1024 × 1024 CCD array using a Gatan GIF imaging parallel electron energy-loss spectrometer attached to a Hitachi HF2000 field emission gun electron miscroscope running at 200 keV. A 10 eV energy window centred around the zero-loss peak in the energy-loss spectrum enabled filtering of plasmon inelastic scattering from the LACBED pattern. Diffuse background left in the pattern was measured by displacing the SAD aperture slightly to exclude elastic scattering. The pattern was then transferred to a VAX workstation for further processing and the diffuse background was subtracted from the diffraction intensity. Thus, the pattern was virtually free of inelastic scattering and ready for comparison with results from the two models.

The intensities of fringe maxima were measured using data obtained by averaging ten pixels along each fringe

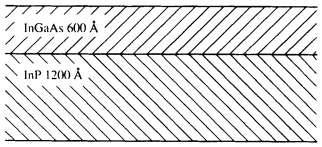

Fig. 4. Schematic cross section of the $In_{0.53}Ga_{0.47}As$/InP bicrystal grown by MOVPE on an InP wafer and thinned with selective etches (H_2SO_4:H_2O_2:H_2O = 1:8:1 for $In_{0.53}Ga_{0.47}As$ and HCl for InP).

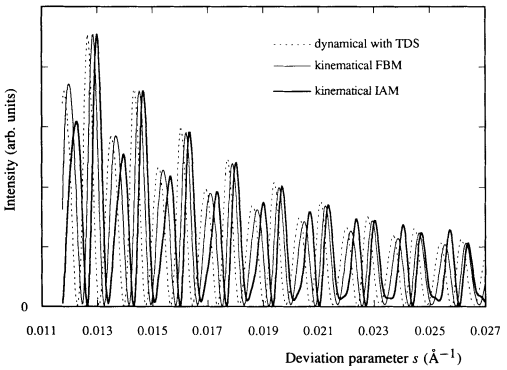

Fig. 5. Rocking curves calculated for the IAM using kinematical theory and for the FBM using both kinematical and dynamical theory based on Bloch waves including 21 beams and absorption due to TDS. The curves are rescaled and displaced horizontally for comparison. Differences for the FBM between the kinematical and dynamical calculations are negligible compared with differences between the kinematical calculations for the FBM and the IAM.

and avoiding perturbations by non-systematic reflections. Simulations based on the kinematical theory of electron diffraction used atomic form factors listed by Doyle & Turner (1968) and Debye–Waller factors at 300 K given by Reid (1983). To ensure kinematical theory is applicable and dynamical effects from systematic reflections and absorption due to TDS are not important, a third simulation based on Bloch-wave theory using an Einstein model for the TDS absorptive potential (Hall & Hirsch, 1965) is displayed in Fig. 5, together with the kinematical calculations. For the boundary conditions, the FBM was assumed. As can be seen, the differences between the dynamical and the kinematical calculations using the FBM are negligible compared with differences between calculations using the FBM and the IAM.

4. Results

A section of the experimental 200 LACBED pattern from the bicrystal is displayed in Fig. 6(*b*) together with simulations for each boundary model in Figs. 6(*a*) and (*c*). A sequence of alternating strong and weak fringes can be seen in all three patterns. Other simulations not presented here showed that, if the layer thickness ratio of 1:2 is not strictly obeyed, the modulation dies away at a certain deviation s and reappears as s increases. This makes it possible to measure the exact thickness ratio of the sample from the experimental pattern. The simulations in Fig. 6 represent best fits to the experimental pattern, and the thickness ratio was found to be within 5% of the target ratio. It is important to note that simulations based on the IAM were sensitive to the layer order and the definition of the unit-cell origin. A different layer order or unit-cell origin changes the stacking sequence of group III and group V layers and gives the sample a different structure. The structure remains the same, however, if the sample is viewed from the opposite side and there are no changes to the kinematical calculations. A good fit was only obtained with the $In_{0.53}Ga_{0.47}As$ layer at the top as shown in Fig. 4 and with the group III atoms at the origin of the unit cell and the group V atoms at fractional coordinates $(\frac{1}{4}, \frac{1}{4}, \frac{1}{4})$.

Before considering intensities, we may observe that the fringe spacing in all three patterns is not constant. The fringes form pairs of two closer fringes separated from the next pair by a larger gap. This is most visible in Fig. 6(*c*), where paired fringes are indicated, and less apparent in Fig. 6(*a*). The experimental pattern in Fig. 6(*b*) shows clear evidence of pairing which suggests better agreement with Fig. 6(*c*) in support of the IAM.

The intensity ratios of adjacent fringe maxima in the experimental and simulated patterns are compared for the first 14 fringes in Table 1. Data from the last two fringes in Fig. 6(*b*) were considered unreliable due to the weak intensity of the fringes, and it was not included for comparison. For most ratios in Table 1, the calculation for the IAM agrees significantly better with the

experiment than that for the FBM. A χ^2 test was performed for each model using the data in Table 1. For the IAM, this gave a value five times lower than for the FBM, clearly indicating better agreement for the IAM.

5. Discussion

It is well known from reflection high-energy electron diffraction (RHEED), low-energy electron diffraction (LEED) and scanning tunnelling microscopy (STM) studies of clean crystal surfaces that the crystal surface is not flat [see Peng & Whelan (1990*b*) for a dynamical treatment of RHEED]. However, the sensitivity of diffraction intensities to details of the structure at surfaces and interfaces in TEM has not been reported before. The simulations presented in Fig. 6 and Table 1 suggest that the diffraction intensity from a thin crystal depends on small differences in the crystal potential at boundaries if a weak reflection at large deviation s from the Bragg peak is considered.

An alternative interpretation of the differences between the FBM and the IAM has been suggested by Preston (1989), which is based on the observation that there is an additional phase change between monolayers of anions and cations within a unit cell when the deviation parameter s is altered. This phase difference is neglected in calculations using the fixed structure factors F_g [(14)], which are independent of s. This explanation leads to the same amplitude and phase changes as described in §2. However, the interpretation is misleading because it renders the changes in Fig. 2 as an effect that occurs in the bulk of the crystal. This is not the case because, as explained in §2, the bulk potential is the same for the FBM and the IAM and, therefore, cannot cause the differences shown in Fig. 2.

Both models presented in §2 ignore formation of two-dimensional superlattices at clean crystal surfaces (sur-

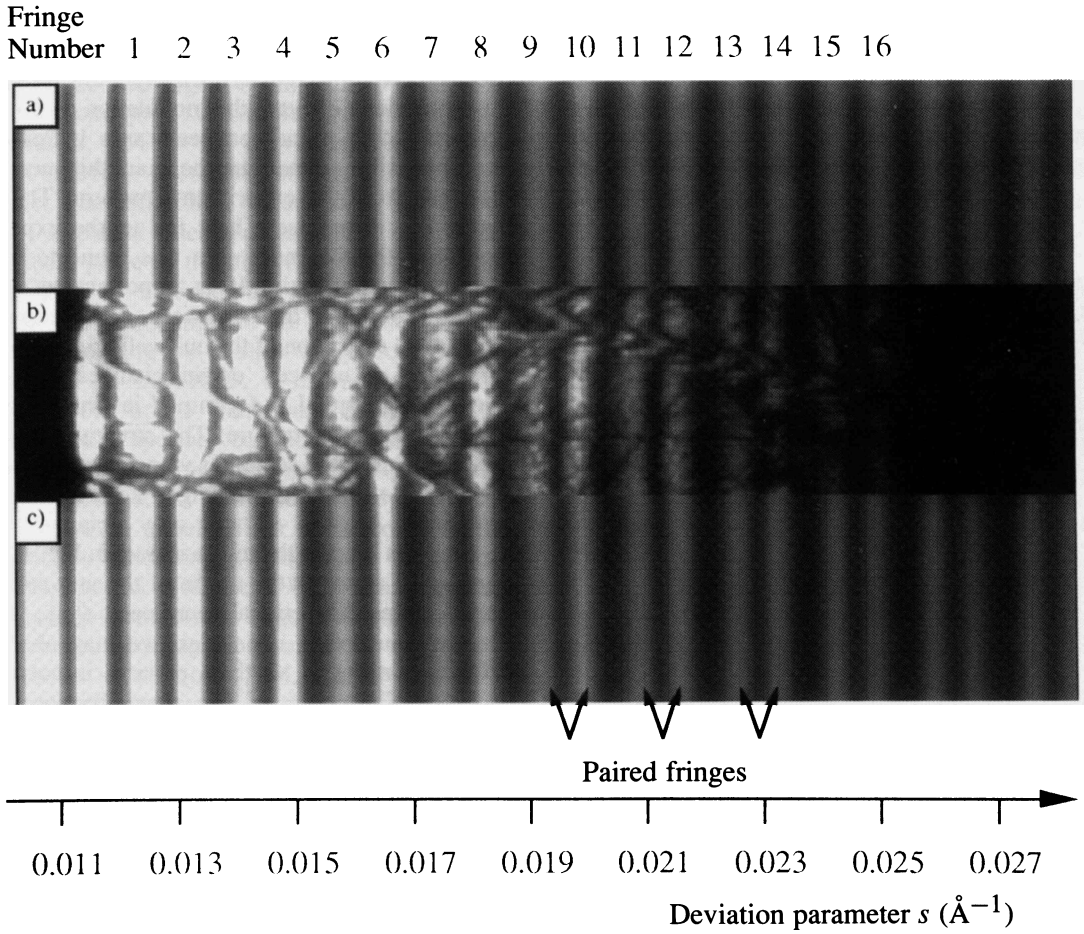

Fig. 6. Simulated and experimental 200 LACBED patterns. In (*a*) the FBM was used to calculate the best fit to the experimental pattern in (*b*). (*c*) shows the same calculation using the IAM. In (*c*), fringes are not equidistant but form pairs of two closer fringes separated from the next pair by a larger gap. The fringes are indicated in the region where pairing is most visible. The pairing can also be seen in the simulation in (*a*) but to a smaller extent. The experimental pattern in (*b*) shows clear evidence of pairing which suggests better agreement with the simulation in (*c*) according to the IAM.

Table 1. *Observed and calculated intensity ratios for adjacent fringe maxima*

The fringes are indicated in the first column with numbers according to Fig. 6. The second and third columns give observed ratios $R_{n,\mathrm{obs}}$ and standard deviations σ_n obtained from intensities and standard deviations of ten pixels measured along each fringe, respectively. The calculated ratios $R_{n,\mathrm{FBM}}$ and $R_{n,\mathrm{IAM}}$ for the FBM and the IAM are listed in columns 4 and 5 together with their deviations from the observed ratios. For most ratios, the deviation for the IAM is significantly smaller than for the FBM. Each model was tested using the χ^2 test with $\chi^2 = \sum_n (R_{n,\mathrm{obs}} - R_{n,\mathrm{sim}})^2/\sigma_n^2$ and values are given at the bottom of the table. The χ^2 value for the IAM is smaller by a factor of five giving clear evidence that the IAM fits the experiment better.

Fringe no.	Observed	σ	FBM	Deviation (%)	IAM	Deviation (%)
1/2	0.676	0.080	0.803	18.8	0.677	0.2
2/3	1.705	0.145	1.602	6.0	1.793	5.2
3/4	0.708	0.052	0.791	11.7	0.703	0.7
4/5	1.628	0.106	1.541	5.3	1.657	1.8
5/6	0.725	0.058	0.805	10.9	0.737	1.6
6/7	1.579	0.186	1.461	7.5	1.534	2.8
7/8	0.816	0.094	0.837	2.5	0.791	3.1
8/9	1.488	0.198	1.374	7.7	1.403	5.7
9/10	0.847	0.130	0.881	4.0	0.863	1.9
10/11	1.316	0.157	1.282	2.5	1.270	3.5
11/12	0.927	0.095	0.935	0.8	0.926	0.1
12/13	1.383	0.189	1.193	13.7	1.176	15.0
13/14	1.013	0.138	0.998	1.5	0.995	1.8
			$\chi^2_{\mathrm{FBM}} = 10.2$		$\chi^2_{\mathrm{FBM}} = 2.1$	

face reconstruction) as shown by Wassermeier *et al.* (1992), Chambers (1992), LaFemina (1992) and Li & Tong (1993) in the case of GaAs. Also, contamination on the surface during sample preparation and handling has been neglected. Small shifts of atom positions at the surface due to reconstruction may change diffraction contrast depending on the magnitude and direction of shift. It has been suggested, however, that absorption of atoms on crystal surfaces is likely to reverse reconstruction by dangling-bond saturation (Newstead *et al.*, 1993; LaFemina, 1992). Thus, it is probable that the position of atoms at the crystal surface is coherent with the bulk structure and diffraction contrast is not changed.

The effect of contamination on image contrast was discussed by Metherell (1967). He assumed an amorphous layer at the entrance surface of the crystal and concluded that the angular distribution of the beam would be widened by the diffuse scattering of the surface layer, thereby reducing the contrast in images. In our case, we look at a LACBED pattern, which is a diffraction pattern. A change in the angular distribution of the beam would only change the angular range visible in the pattern while intensities would remain unchanged. However, diffuse scattering by an amorphous layer at the exit surface of the crystal would, to some extent, average intensities of beams travelling in different directions, and hence contrast in the LACBED pattern would be reduced. It is not known whether there is a reduction of diffraction contrast due to contamination in patterns shown in §4, but the experimental pattern displays contrast that is stronger (*cf.* intensity ratios in Table 1) than that predicted by the FBM and is, therefore, in closer agreement with the IAM. Hence, the averaging effect must be small. Correction of experimental intensities should cause worse agreement with calculations based on the FBM and better agreement with the IAM.

6. Concluding remarks

Kinematical calculations based on both the flat-boundary model and the independent-atom model have been compared with experimental observations. The two models show differing diffraction amplitudes and phases in case of weak low-order reflections (*e.g.* 200 in InGaAs) which are greater at large deviation from the Bragg peak and negligible at small deviation where scattering is dynamical. An energy-filtered large-angle convergent-beam electron diffraction pattern in the 200 reflection from an $In_{0.53}Ga_{0.47}As/InP$ bicrystal was recorded under kinematical conditions and compared with simulations using the two models. A comparison of fringe position and a quantitative analysis of intensities in the diffraction pattern showed the simulation using the IAM agrees better with experiment, suggesting that this model represents the true crystal potential at surfaces and interfaces more accurately.

This work would not have been possible without the help of BT Laboratories who provided financial support and the sample grown by S. D. Perrin and P. B. Webb. The authors are grateful to R. Vincent for his constant support throughout the project and D. M. Bird, R. D. Grigorieff, M. J. Whelan and W. M. Stobbs for helpful discussions and comments on the theory presented here.

APPENDIX
Derivation of equation (11)

We consider a sum of N δ functions, N odd

$$f(z) = \sum_{n=0}^{N-1} \delta\{z + [(N-1)/2]c - nc\}, \tag{18}$$

which has the Fourier transform

$$\begin{aligned} f(q_z) &= \exp[-\pi i q_z (N-1)c] \sum_{n=0}^{N-1} \exp(2\pi i q_z nc) \\ &= \exp[-\pi i q_z (N-1)c] \frac{\exp(2\pi i q_z Nc) - 1}{\exp(2\pi i q_z c) - 1} \\ &= \sin(\pi q_z Nc)/\sin(\pi q_z c). \end{aligned} \tag{19}$$

On the other hand, we may write (18) as an infinite sum of δ functions limited by a slit function $S(z)$ of width Nc and the origin in the middle:

$$f(z) = S(z) \sum_{n=-\infty}^{\infty} \delta(z - nc). \tag{20}$$

The Fourier transform is then given as

$$f(q_z) = S(q_z) * \sum_n \exp(2\pi i q_z nc)$$
$$= [\sin(\pi q_z Nc)/\pi q_z] * c^{-1} \sum_{g_z} \delta(q_z - g_z)$$
$$= \sum_{g_z} \sin[\pi(q_z - g_z)Nc]/\pi(q_z - g_z)c. \qquad (21)$$

Equation (21) is identical with (19) since (18) equals (20) and hence

$$\sum_{g_z} \frac{\sin[\pi(q_z - g_z)Nc]}{\pi(q_z - g_z)c} = \frac{\sin(\pi q_z Nc)}{\sin(\pi q_z c)}. \qquad (22)$$

References

ANSTIS, G. R. & COCKAYNE, D. J. H. (1979). *Acta Cryst.* A**35**, 511–524.

BETHE, H. (1928). *Ann. Phys. (Leipzig)*, **87**, 55–129.

CHAMBERS, S. A. (1992). *Surf. Sci. Rep.* **16**, 261–331.

DOYLE, P. A. & TURNER, P. S. (1968). *Acta Cryst.* A**24**, 390–397.

GIPSON, J. M., LANZEROTTI, M. Y. & ELSER, V. (1989). *Appl. Phys. Lett.* **55**, 1394–1396.

GRIGORIEFF, N., CHERNS, D., YATES, M. J., HOCKLY, M., PERRIN, S. D. & AYLETT, M. R. (1993). *Philos. Mag.* A**68**, 121–136.

HALL, C. R. & HIRSCH, P. B. (1965). *Proc. R. Soc. London Ser. A*, **286**, 158–177.

HARGITTAI, I. (1988). *Stereochemical Applications of Gas-Phase Electron Diffraction*, Part A, edited by I. HARGITTAI & M. HARGITTAI, pp. 1–54. New York: VCH Publishers Inc.

JORDAN, I. K., CHERNS, D., HOCKLY, M. & SPURDENS, P. C. (1989). *Inst. Phys. Conf. Ser.* No. 100, pp. 293–298.

JORDAN, I. K., ROSSOUW, C. J. & VINCENT, R. (1991). *Ultramicroscopy*, **35**, 237–243.

LAFEMINA, J. P. (1992). *Surf. Sci. Rep.* **16**, 133–260.

LI, H. & TONG, S. Y. (1993). *Surf. Sci.* **282**, 380–388.

METHERELL, A. J. F. (1967). *Philos. Mag.* **15**, 763–776.

NEWSTEAD, K., ROBINSON, A. W., D'ADDATO, S., PATCHETT, A., PRINCE, N. P., MCGRATH, R., WHITTLE, R., DUDZIK, E. & MCGOVERN, I. T. (1993). *Surf. Sci.* **287/288**, 317–320.

PENG, L.-M. & WHELAN, M. J. (1990*a*). *Proc. R. Soc. London Ser. A*, **431**, 111–123.

PENG, L.-M. & WHELAN, M. J. (1990*b*). *Proc. R. Soc. London Ser. A*, **431**, 125–142.

PRESTON, A. R. (1989). PhD thesis, Univ. of Bristol, England.

REID, J. S. (1983). *Acta Cryst.* A**39**, 1–13.

STOBBS, S. H., BOOTHROYD, C. B. & STOBBS, W. M. (1989). *Inst. Phys. Conf. Ser.* No. 98, pp. 387–390.

TANAKA, M., SAITO, R., UENO, K. & HARADA, Y. (1980). *J. Electron Microsc.* **29**, 408–412.

VINCENT, R. (1989). *J. Electron Microsc. Tech.* **13**, 40–50.

WASSERMEIER, M., BRESSLER-HILL, V., MABOUDIAN, R., POND, K., WANG, X.-S., WEINBERG, W. H. & PETROFF, P. M. (1992). *Surf. Sci. Lett.* **278**, 147–151.

ZUO, J. M., SPENCE, J. C. H. & O'KEEFFE, M. (1988). *Phys. Rev. Lett.* **61**, 353–356.